Variational Iterative Algorithms in Photoacoustic Tomography with Variable Sound Speed

Tangjie Lv*and Tie Zhou†
LMAM, School of Mathematical Sciences, Peking University ‡

Abstract

In this paper, we investigate the adjoint equation in photoacoustic tomography with variable sound speed, and propose three variational iterative algorithms. The basic idea of these algorithms is to compute the original equation and the adjoint equation iteratively. We present numerical examples and show the well performance of these variational iterative algorithms.

1 Introduction

Photoacoustic Tomography or Thermoacoustic Tomography is a developing medical imaging method in recent decades [24]. They are hybrid medical imaging methods characterized by high resolution and contrast. The physical principle can be described as follows. Light or a short electromagnetic energy irradiates the biological tissue and the energy is absorbed by the tissue. The tissue heats up and results in the phenomenon of the thermal expansion. This expansion leads to weak acoustic waves and these waves are measured by ultrasound transducers located on an observation surface. The measured information is used to recover the initial acoustic pressure, which is roughly proportional to the rate of absorption [24]. Then the initial acoustic pressure is used to produce an image.

We describe the widely accepted mathematical model here [12, 17]. Let $\Omega \subset \mathcal{R}^n$ be an open set with a smooth boundary, in applications, $n = 2, 3$. Assume that the sound speed $c(x)$ is smooth, strictly positive and $c(x) = 1$ outside Ω. Suppose $u(x, t)$ is the solution of the wave equation

$$\begin{cases} u_{tt} - c^2\Delta u &= 0, \quad t \geq 0,\ x \in \mathcal{R}^n \\ u|_{t=0} &= f \\ u_t|_{t=0} &= 0 \end{cases} \tag{1}$$

in which the function f is supported in Ω and the value of u could be collected at transducer's location $x \in S$ before a fixed measuring time T, where $S \subset \partial\Omega$ is the closed observation surface. The measured value could be modeled by an operator as follows

$$\mathbf{K}f := u|_{S\times[0,T]} \tag{2}$$

The image reconstruction problem in photoacoustic tomography is to recover the initial value $f(x)$ by using the measured value $\mathbf{K}f$

*Electronic address: lvtangjie@gmail.com
†Electronic address: tzhou@math.pku.edu.cn
‡This work is supported by the National Basic Research Program of China (2011CB809105) and NSF grants of China (61121002, 10990013).

Obviously, this is an inverse problem. A lot of work have been done when the sound speed $c(x)$ is constant and $S = \partial\Omega$, and there are various types of reconstruction methods to solve this problem (e.g filtered backprojection formulas, eigenfunction expansions and time reversal). Actually, when $n = 3$ and the observation surface is spherical surface, the first inversion formula has been found in [6]. Then in [23], a universal inversion formula has been proposed in the case of the observation surface being spherical, planar and cylinadrical surface. The eigenfunction expansion methods can work for any closed observation surface with constant sound speed and the algorithm reconstructs the image faster than filtered backprojection formulas. However, all of them would not be efficient for variable sound speed [2, 13, 14]. There are many cases that the sound speed is variable [25]. If we apply the reconstruction methods for constant speed on the variable sound speed condition, which use the average sound speed as the constant sound speed, it may cause large image errors [9]. Therefore, designing an effecient algorithm for photoacoustic tomography with variable sound speed is an important work.

Several image reconstruction methods have been proposed to compensate for weak sound speed variations. These methods assume that the photoacoustic wavefields propagate along well-defined geometrical acoustic rays [16, 25]. However, these models possess limitations. The ray-based propagation models will be effective only on length scales that are large compared to the effective acoustic wavelength. These assumptions can be voilated in preclinical and clinical applications [10].

For strong sound speed variations, the time reversal method has been proposed and it works well in numerical experiments when the measuring time T is large enough, though it gives the exact reconstruction result only when the sound speed is constant and the dimension is odd [4, 9, 8, 26]. If these conditions are not simultaneously satisfied, it gives the approximate results [8, 9], and the errors will increase when T becomes small [8, 17]. The Neumann series method is derived in [20, 21] and is proved to be an exact reconstruction method under the variable sound speed circumstance, even though T is not large. This method has been validated effecitve in numerical experiments [17]. In [3], the authors study the adjoint operator of the appoximate photoacoustic tomography model with constant sound speed and propose a conjugate gradient method. They use this method on the variable sound speed condition in numerical experiments. When T is fixed, the conjugate gradient method performs better than time reversal, but worse than Neumann series [3].

In this paper, we investigate the adjoint operator of the exact photoacoustic tomography model with variable sound speed, and propose three variational iterative algorithms. We present numerical examples and show that the proposed algorithms performs better than time reversal and Neumann series, especially with noisy data.

This paper is organized as follows. In Section 2, we introduce some basic theories of the hyperbolic equation. The adjoint of the imaging operator and the adjoint equation are studied in Section 3. In Section 4, three variational iterative algorithms based on the adjoint operator are proposed. Finally, numerical results are presented in Section 5, showing that our proposed approaches reconstruct the better results than existing methods.

2 Preliminaries

Assume $f \in C_0^\infty(\Omega)$, $c(x) \in C^\infty(\mathcal{R}^n)$, and u is the smooth solution of the equation (1), then according to the finite propagation speed theorem [5], there exists a ball $U = B(0, R), \Omega \subset U$ that u is supported in U between time 0 and T. Therefore, we can study

the following the initial/boundary-value problem instead of the equation (1)

$$\begin{cases} u_{tt} - c^2\Delta u &= 0, \quad (x,t) \in U \times [0,T] \\ u|_{t=0} &= f \\ u_t|_{t=0} &= 0 \\ u &= 0, \quad x \in \partial U \end{cases} \tag{3}$$

It is clear that if u is the smooth solution of the equation (1), it must be the solution of the equation (3).

Let us study a general initial/boundary-value problem

$$\begin{cases} u_{tt} - c^2\Delta u &= h(x,t), \quad (x,t) \in U \times (0,T) \\ u|_{t=0} &= f(x) \\ u_t|_{t=0} &= g(x) \\ u &= 0, \qquad x \in \partial U \end{cases} \tag{4}$$

We introduce the time-dependent bilinear form

$$B[u,v;t] := \int_U (c^2 \nabla u \cdot \nabla v + \sum_{i=1}^{n} 2cc_{x_i} u_{x_i} v) dx$$

for $u, v \in H_0^1(U)$ and $0 \le t \le T$. We say a function $u \in L^2(0,T;H_0^1(U))$, with $u_t \in L^2(0,T;L^2(U))$, $u_{tt} \in L^2(0,T;H^{-1}(U))$ is a weak solution of the equation (4) provided

$$\begin{cases} \int_U u_{tt} v dx + B[u,v;t] &= \int_U hv dx \\ & \quad \forall v \in H_0^1(U) \text{ and a.e. } 0 \le t \le T \\ u(x,0) &= f \\ u_t(x,0) &= g \end{cases} \tag{5}$$

Theorem 2.1 *[5]*
Assume $f \in H_0^1(U), g \in L^2(U), h \in L^2(0,T;L^2(U))$, then there exists a unique weak solution of the equation (4). In fact

$$u \in L^\infty(0,T;H_0^1(U)), u_t \in L^\infty(0,T;L^2(U)),$$

and we have the estimate

$$\begin{aligned} &\text{ess sup}_{0 \le t \le T}(||u(t)||_{H_0^1(U)} + ||u_t(t)||_{L^2(U)}) \\ &\le C(||f||_{H_0^1(U)} + ||g||_{L^2(U)} + ||h||_{L^2(0,T;L^2(U))}) \end{aligned}$$

Theorem 2.2 *[5]*
Assume $f, g \in C^\infty(\bar{U})$, $h \in C^\infty(\bar{U}_T)$, and the $m^{th}-$order compatibility conditions hold for $m = 0, 1, \cdots$

$$\begin{cases} f_0 := f \in H_0^1(U), \ g_1 := g \in H_0^1(U) \\ f_{2l} := \frac{d^{2l-2}h}{dt^{2l-2}}(\cdot,0) - Lf_{2l-2} \in H_0^1(U) \qquad (if\ m = 2l) \\ g_{2l+1} := \frac{d^{2l-1}h}{dt^{2l-1}}(\cdot,0) - Lg_{2l-1} \in H_0^1(U) \quad (if\ m = 2l+1) \end{cases}$$

the equation (4) has a unique solution

$$u \in C^\infty(\bar{U}_T)$$

If $f \in C_0^\infty(\Omega)$, then $f \in C_0^\infty(U)$. According to Theorem 2.2, the equation (3) has a unique smooth solution $\bar{u}$. Assume u is the smooth solution of the equation (1), thus

$$u = \bar{u}, \quad (x,t) \in \bar{U} \times [0,T]$$

3 Variational Approach

Define an operator $\mathbf{W}$

$$\begin{array}{rcl} \mathbf{W} : H_0^1(\Omega) & \longrightarrow & L^2(0,T;H_0^1(U)) \\ f & \longmapsto & u \end{array}$$

where u is the weak solution of the equation (3). Next, we define a projection operator $\mathbf{P}$

$$\begin{array}{rcl} \mathbf{P} : L^2(0,T;H_0^1(U)) & \longrightarrow & L^2(0,T;L^2(S)) \\ u & \longmapsto & u|_{S\times[0,T]} \end{array}$$

Then the forward operator $\mathbf{K}$ can be expressed $\mathbf{K} := \mathbf{PW}$

$$\begin{array}{rcl} \mathbf{K} : H_0^1(\Omega)) & \longrightarrow & L^2(0,T;L^2(S)) \\ f & \longmapsto & u|_{S\times[0,T]} \end{array}$$

We first prove that the operator $\mathbf{K}$ is a linear bounded operator from space $H_0^1(\Omega)$ to space $L^2(0,T;L^2(S))$. It is clear that this operator is a linear operator. Therefore, we only need to prove the boundedness. Use the inequality in Theorem 2.1

$$\begin{array}{ll} ||\mathbf{K}f||_{L^2(0,T;L^2(S))} & \leq ||u||_{L^2(0,T;L^2(\partial\Omega))} \\ & \leq ||u||_{L^2(0,T;H^1(\Omega))} \\ & \leq ||u||_{L^2(0,T;H_0^1(U))} \\ & \leq C||f||_{H_0^1(U)} \\ & = C||f||_{H_0^1(\Omega)} \end{array}$$

If we have the value $p(x,t)$ on S between time 0 and T, the we can solve the inverse problem

$$f = arg \min_{f\in H_0^1(\Omega)} ||\mathbf{K}f - p||^2_{L^2(0,T;L^2(S))} \tag{6}$$

Therefore we need to look for the adjoint operator $\mathbf{K}^*$ to solve this inverse problem. Here, we introduce a special equation, which we call the adjoint equation of the equation (3)

$$\left\{ \begin{array}{rcll} u^*_{tt} - c^2\Delta u^* & = & p(x,t)\delta(S), & (x,t) \in S \times (0,T) \\ u^*|_{t=T} & = & 0 & \\ u^*_t|_{t=T} & = & 0 & \\ u^* & = & 0, & x \in \partial U \end{array} \right. \tag{7}$$

where $S \in \partial\Omega, \Omega \subset U$ and $p(x,t) \in L^2(0,T;L^2(S))$. $\delta(S)$ is defined as follows

$$\int_U \phi\delta(S)dx = \int_S \phi ds(x), \forall \phi \in H_0^1(U)$$

Before define the weak solution of the adjoint equation, we first define a test function set

$$\begin{aligned}\mathcal{D} := \{v | & v \text{ is a weak solution of the equation (4)};\\ & h \in L^2(0,T;L^2(U)),\ f \in H_0^1(U),\ g \in L^2(U)\}\end{aligned}$$

It is obvious that $C^2([0,T];C_0^2(U)) \subset \mathcal{D}$. Since $C^2([0,T];C_0^2(U))$ is dense in $L^2(0,T;H_0^1(U))$, $\mathcal{D}$ is dense in $L^2(0,T;H_0^1(U))$.

We say $u^* \in L^2(0,T;L^2(U))$ with $u^*(x,0) \in L^2(U)$, $u_t^*(x,0) \in H^{-1}(U)$ is a weak solution of the equation (7) provided

$$\begin{aligned}&\int_0^T \int_U c^{-2}u^* h dx dt - \int_U c^{-2}u_t^*(x,0) f dx + \int_U c^{-2}u^*(x,0) g dx\\ &= \int_0^T \int_S c^{-2} p v ds(x) dt, \forall v \in \mathcal{D}\end{aligned} \tag{8}$$

Theorem 3.1 *Assume $p(x,t) \in L^2(0,T;L^2(S))$, then there exists a unique weak solution $u^* \in L^2(0,T;L^2(U))$ with $u^*(x,0) \in L^2(U)$, $u_t^*(x,0) \in H^{-1}(U)$ of the equation (7), and we have the estimate*

$$\begin{aligned}&||u^*||_{L^2(0,T;L^2(U))} + ||u^*(x,0)||_{L^2(U)} + ||u_t^*(x,0)||_{H^{-1}(U)}\\ &\le C||p(x,t)||_{L^2(0,T;L^2(S))}\end{aligned}$$

Proof. Let us introduce three subsets in $\mathcal{D}$

$$\begin{aligned}\mathcal{D}_1 &:= \{v | h \in L^2(0,T;L^2(U)),\ f = 0,\ g = 0\}\\ \mathcal{D}_2 &:= \{v | h = 0,\ f \in H_0^1(U),\ g = 0\}\\ \mathcal{D}_3 &:= \{v | h = 0,\ f = 0,\ g \in L^2(U)\}\end{aligned}$$

It is easy to show that $\mathcal{D}_1 \subset \mathcal{D}$, $\mathcal{D}_2 \subset \mathcal{D}$, $\mathcal{D}_3 \subset \mathcal{D}$.

First, we prove that there exist a unique solution $u^*(x,t) \in L^2(0,T;L^2(U))$ when the test function $v \in \mathcal{D}_1$. For a given function $h \in L^2(0,T;L^2(U))$, there exists $v_1 \in \mathcal{D}_1$ that

$$\int_0^T \int_U c^{-2}u^* h dx dt = \int_0^T \int_S c^{-2} p v_1 ds(x) dt \tag{9}$$

According to Theorem 2.1

$$\begin{aligned}\int_0^T \int_S c^{-2} p v_1 ds(x) dt &\le ||p||_{L^2(0,T;L^2(S))}||v_1||_{L^2(0,T;L^2(S))}\\ &\le ||p||_{L^2(0,T;L^2(S))}||v_1||_{L^2(0,T;L^2(\partial\Omega))}\\ &\le C_1||p||_{L^2(0,T;L^2(S))}||v_1||_{L^2(0,T;H^1(\Omega))}\\ &\le C_1||p||_{L^2(0,T;L^2(S))}||v_1||_{L^2(0,T;H_0^1(U))}\\ &\le C_2||p||_{L^2(0,T;L^2(S))}||h||_{L^2(0,T;L^2(U))}\end{aligned}$$

Then the right side of the equation (9) is a linear functional on $L^2(0,T;L^2(U))$. According to *Rieze* Theorem, there exist a unique $u^* \in L^2(0,T;L^2(U))$.

Using the same proof process, we can get a unique function $u_t^*(x,0) \in H^{-1}(U)$, $u^*(x,0) \in L^2(U)$, which we use the test function sets $\mathcal{D}_2$, $\mathcal{D}_3$.

Next we prove that $\forall v \in \mathcal{D}$, we have the equation (8). We first prove that for a given $v_0 \in \mathcal{D}$, there exists $v_1 \in \mathcal{D}_1$, $v_2 \in \mathcal{D}_2$, $v_3 \in \mathcal{D}_3$ that

$$v_0 = v_1 + v_2 + v_3$$

Since $v_0 \in \mathcal{D}$, there exists $h_0 \in L^2(0,T;L^2(U))$, $f_0 \in H_0^1(U)$, $g_0 \in L^2(U)$ that v_0 is the weak

solution of the equation

$$\begin{cases} v_{tt} - c^2\Delta v &= h_0, \quad (x,t) \in U \times (0,T) \\ v|_{t=0} &= f_0 \\ v_t|_{t=0} &= g_0 \\ v &= 0, \quad x \in \partial U \end{cases} \tag{10}$$

Assume v_1 is the weak solution of the equation

$$\begin{cases} v_{tt} - c^2\Delta v &= h_0, \quad (x,t) \in U \times (0,T) \\ v|_{t=0} &= 0 \\ v_t|_{t=0} &= 0 \\ v &= 0, \quad x \in \partial U \end{cases} \tag{11}$$

Assume v_2 is the weak solution of the equation

$$\begin{cases} v_{tt} - c^2\Delta v &= 0, \quad (x,t) \in U \times (0,T) \\ v|_{t=0} &= f_0 \\ v_t|_{t=0} &= 0 \\ v &= 0, \quad x \in \partial U \end{cases} \tag{12}$$

Assume v_3 is the weak solution of the equation

$$\begin{cases} v_{tt} - c^2\Delta v &= 0, \quad (x,t) \in U \times (0,T) \\ v|_{t=0} &= 0 \\ v_t|_{t=0} &= g_0 \\ v &= 0, \quad x \in \partial U \end{cases} \tag{13}$$

According to Theorem 2.1, there exist $v_1 \in \mathcal{D}_1$, $v_2 \in \mathcal{D}_2$, $v_3 \in \mathcal{D}_3$. Write $\bar{v} = v_1 + v_2 + v_3$, then $\bar{v}$ is the weak solution of the equation (10), thus

$$v_0 = \bar{v} = v_1 + v_2 + v_3$$

Then we have

$$\begin{aligned} &\int_0^T \int_U c^{-2} u^* h dx dt - \int_U c^{-2} u_t^*(x,0) f dx + \int_U c^{-2} u^*(x,0) g dx \\ &= \int_0^T \int_S c^{-2} p v_0 ds(x) dt, \forall v_0 \in \mathcal{D} \end{aligned}$$

For a given $f \in H_0^1(\Omega)$, assume v is the weak solution of the equation (3), we have

$$\begin{aligned} \int_U -c^{-2} u_t^*(x,0) f dx &= \int_0^T \int_S c^{-2} p v ds(x) dt \\ &= \int_0^T \int_S p v ds(x) dt, \forall f \in H_0^1(\Omega) \end{aligned}$$

Define

$$\mathbf{K}^* p = -c^{-2} u_t^*(x,0)$$

Thus

$$< \mathbf{K}^* p, f >= (p, \mathbf{K} f)$$

4 Iterative Algorithms

4.1 Landweber Iteration

The Landweber iteration has been proposed in [7, 15], the authors suggest rewriting the equation $\mathbf{K}f = g$ in the form $f = (\mathbf{I} - \tau\mathbf{K}^*\mathbf{K})f + \tau\mathbf{K}^*g$ for some $\tau > 0$ and iterating this equation

$$\begin{aligned} &f_0 := \textit{initial guess} \\ &f_n = (\mathbf{I} - \tau\mathbf{K}^*\mathbf{K})f_{n-1} + \tau\mathbf{K}^*g \end{aligned}$$

for $n = 1, 2, \cdots$. This iteration scheme can be interperted as the steeptest descent algorithm applied to the quadratic functional [11]

$$J(f) = ||\mathbf{K}f - g||^2 \tag{14}$$

4.2 Conjugate Gradient Method

A fast iterative algorithm for solving least squares problems is the conjugate gradient method [11]

$n := 0;$
$f_0 := 0;$
$p_0 := -\mathbf{K}^*g$
begin conjugate gradient method
  $t_n = \frac{(\mathbf{K}f_n - g, \mathbf{K}p_n)}{\|\mathbf{K}p_n\|};$
  $f_{n+1} = f_n - t_n p_n;$
  $\alpha_n = \frac{\|\mathbf{K}^*(\mathbf{K}f_{n+1} - g)\|^2}{\|\mathbf{K}^*(\mathbf{K}f_n - g)\|^2};$
  $p_{n+1} = \mathbf{K}^*(\mathbf{K}f_{n+1} - g) + \alpha_n p_n;$
  $n = n + 1;$
end conjugate gradient method

4.3 Total Variation Regularization

If the original image f is nearly piecewise constant with jump discontinuities, we can minimize the Tikhonov-TV functional [1, 22]

$$T_\alpha(f) = \frac{1}{2}||\mathbf{K}f - g||^2 + \alpha TV(f) \tag{15}$$

where

$$TV(f) := \sup_{\overrightarrow{v} \in \mathcal{V}} \int_\Omega f \mathrm{div}\, \overrightarrow{v}\, dx,$$

and the space of the functions

$$\mathcal{V} = \{\overrightarrow{v} \in C_0^1(\Omega) |\ |\overrightarrow{v}(x)| \leq 1 \ \textit{for all}\ x \in \Omega\}$$

The algorithm based on the steepest descent method to solve the equation (15) is given

as follows [19, 22]

$$
\begin{aligned}
&n := 0;\\
&f_0 := \textit{initial guess};\\
&\textit{begin steepest descent iterations}\\
&\quad h_n = \mathbf{K}^*(\mathbf{K}f_n - g) + \alpha\mathbf{L}(f_n)f_n;\\
&\quad f_{n+1} = f_n - \tau h_n;\\
&\quad n = n + 1;\\
&\textit{end steepest descent iterations}
\end{aligned}
$$

where $\alpha > 0, \tau > 0$, and

$$\mathbf{L}(f)f = -\nabla \cdot (\psi'(|\nabla f|^2)\nabla f)$$

with $\psi(t) = 2\sqrt{t + \beta^2}$, where β is a small positive parameter. In our experiments, we choose $\beta = 10^{-7}$.

5 Numerical Experiments

In this section, we use the abbreviation OI for the original image, TR for time reversal, NS for Neumann series, LI for Landweber iteration, CG for conjugate gradient method and TV for total variation regularization, and will only show the two dimensional numerical examples for reducing the cost of the computation. Set $\Omega = [-1.28, 1.28]^2$ and assume that the observation surface S is $\partial\Omega$. We work with three sound speeds, including constant sound speed c_1, non-trapping sound speed c_2 and trapping sound speed c_3.

$$
\begin{aligned}
c_1(x) &= 1.0\\
c_2(x) &= \begin{cases} 1.0 + 0.2sin(2\pi x) + 0.1cos(2\pi y), & x \in \bar{\Omega}\\ 1.0, & x \in \mathbf{R^n}\backslash\bar{\Omega} \end{cases}\\
c_3(x) &= \begin{cases} 0.5, & |x| \le 0.5\\ |x|, & 0.5 < |x| \le 1\\ 1.0, & |x| > 1 \end{cases}
\end{aligned}
$$

To avoid committing an 'inverse crime', a 512×512 grid with $\Delta x_d = \Delta y_d = 0.005$, $\Delta t_d = 0.5\Delta x_d / \max\{c(x)\}$ is employed to generate the measurement data. Then we use mesh sizes $\Delta x = \Delta y = 0.01$, $\Delta t = 2\Delta t_d$ for reconstructions. The iterative parameter τ is set 1 for LI and TV. The regularization parameter α is set 5×10^{-5} for noiseless data, 3×10^{-4} for 10% noise and 5×10^{-4} for 20% noise. All the initial values in LI, CG and TV in the iterations are set 0.

The difficulty of computing the adjoint equation (7) is to compute the function $g(x,t)\delta(S)$. Since the observation surface S is $\partial\Omega$ and $\Delta x = \Delta y$

$$
\begin{aligned}
\textstyle\int_{R^n} g(x,t)\delta(S)dx &\approx \sum_{x_{i,j}} g_{i,j}\delta(S)_{i,j}\Delta x\Delta x\\
\textstyle\int_S g(x,t)ds(x) &\approx \sum_{x_{i,j}\in S} g_{i,j}\Delta x
\end{aligned}
$$

Then $\delta(S)$ can be approximately computed

$$\delta(S) \approx \begin{cases} 0, & x_{i,j} \notin S\\ \frac{1}{\Delta x}, & x_{i,j} \in S \end{cases}$$

Therefore, the adjoint equation (7) can be computed

$$\begin{cases} (\partial_{tt} - c^2\Delta)u^*_{i,j}(t) &= \frac{g_{i,j}(t)}{\Delta x}, & x_{i,j} \in S \\ (\partial_{tt} - c^2\Delta)u^*_{i,j}(t) &= 0, & x_{i,j} \notin S \\ u^*_{i,j}(T) &= 0 \\ \partial_t u^*_{i,j}(T) &= 0 \end{cases}$$

To improve the computation accuracy

$$-u^*_t(\cdot, 0) = \frac{u^*(\cdot, -\Delta t) - u^*(\cdot, \Delta t)}{2\Delta t}$$

It has been suggested in [3, 18] that we can use an arificial numerical atteuation to offset spurious high-frequency effects and noise. Then the wave equation can be computed as follows

$$\frac{u_{n+1} - 2u_n + u_{n-1}}{\Delta t^2} - c^2\Delta u_n = (\Delta x)^\gamma \Delta(\frac{u_n - u_{n-1}}{\Delta t})$$

In our experiments, we set $\gamma = 1.8$.

Finally, we give the computation of the function $\mathbf{L}(f^n)f^n$ in TV [19]

$$\begin{aligned}(\mathbf{L}(f^n)f^n)_{ij} = \quad & -\tfrac{1}{\delta x}[\Delta^x_-(\tfrac{\Delta^x_+ f^n_{ij}}{\sqrt{(\Delta^x_+ f^n_{ij})^2 + (m(\Delta^y_+ f^n_{ij}, \Delta^y_- f^n_{ij}))^2 + \beta^2}}) \\ & + \Delta^y_-(\tfrac{\Delta^y_+ f^n_{ij}}{\sqrt{(\Delta^y_+ f^n_{ij})^2 + (m(\Delta^x_+ f^n_{ij}, \Delta^x_- f^n_{ij}))^2 + \beta^2}})]\end{aligned}$$

where $m(a, b) = minmod(a, b)$ and

$$\begin{aligned}\Delta^x_- f_{ij} &= f_{ij} - f_{i-1,j} \\ \Delta^x_+ f_{ij} &= f_{i+1,j} - f_{ij}\end{aligned}$$

and similarly for $\Delta^y_- f_{ij}$, $\Delta^y_+ f_{ij}$.

In this section, three phantoms are selected to test these algorithms, see Figure 1. In our experiments, we show the numerical results both with noiseless and noisy data, where 10% and 20% additive white Gaussian noise respect to the maximum value of noiseless data are added to the simulated data. In order to compare the performances of these different algorithms, the best reconstructions are adopted by selecting the term numbers in NS, iterative steps in LI, CG and TV in different situations, for the computation errors will increase if we take too many terms or iterative steps.

5.1 Sound Speed c_1

We start with the constant sound speed and reconstruct Phantom 1 and Phantom 3. We set $T = 2$ and use $U = [-3.5, 3.5]^2$ as the computation domain.

The reconstructions and Y-slice diagrams of Phantom 1 with noiseless data are presented in Figure 2, where we take 6 terms in NS, 13 iterative steps in LI, 5 iterative steps in CG and 15 iterative steps in TV. Figure 3 shows the reconstructions and Y-slice diagrams of Phantom 1 with 20% noise, where we take 2 terms in NS, 5 iterative steps in LI, 2 iterative steps in CG and 8 iterative steps in TV.

The reconstructions and Y-slice diagrams of Phantom 3 with noiseless data are presented in Figure 4, where we take 4 terms in NS, 8 iterative steps in LI, 3 iterative steps in CG and 8 iterative steps in TV. Figure 5 shows the reconstructions and Y-slice diagrams of Phantom 3 with 20% noise, where we take 2 terms in NS, 6 iterative steps in LI, 2 iterative steps in

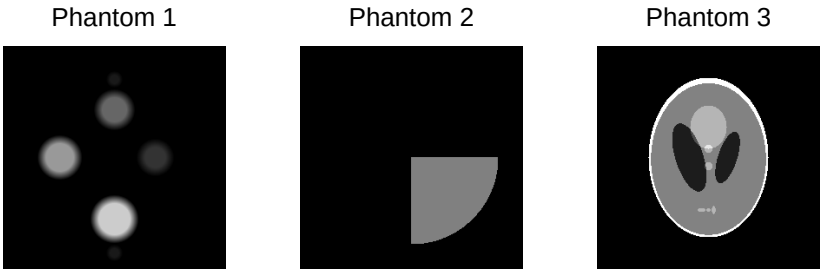

Figure 1: Original Images

Phantom	Noise	TR	NS	LI	CG	TV
Phantom 1	noiseless data	29.1%	3.7%	3.6%	3.5%	3.3%
	10% noise	29.4%	13.8%	11.9%	11.5%	7.4%
	20% noise	30.2%	21.7%	20.2%	20.0%	13.2%
Phantom 3	noiseless data	43.9%	26.0%	23.4%	23.4%	23.3%
	10% noise	44.1%	28.6%	25.8%	25.8%	23.8%
	20% noise	43.9%	31.9%	31.2%	30.6%	27.5%

Table 1: L^2 error in sound speed c_1

CG and 7 iterative steps in TV.

The L^2 errors of these methods in sound speed c_1 are presented at Table 1. We can see that the reconstructions of Phantom 1 are much better than those of Phantom 3, especially in the noisy case. The reason is that Phantom 1 has smooth boundaries between objects while Phantom 3 has discontinuous boundaries, and computing the hyperbolic equation with the discontinuous initial value can cause large computing errors.

5.2 Sound Speed c_2

We still reconstruct Phantom 1 and Phantom 3 in sound speed c_2. Set $T = 2$ and use $U = [-3.5, 3.5]^2$ as the computation domain.

The reconstructions and Y-slice diagrams with noiseless data are presented in Figure 6, where we take 6 terms in NS, 13 iterative steps in LI, 6 iterative steps in CG and 14 iterative steps in TV. Figure 7 shows the reconstructions and Y-slice diagrams with 20% noise, where we take 3 terms in NS, 6 iterative steps in LI, 3 iterative steps in CG and 8 iterative steps in TV.

The reconstructions and Y-slice diagrams of Phantom 3 with noiseless data are presented in Figure 8, where we take 4 terms in NS, 8 iterative steps in LI, 3 iterative steps in CG and 8 iterative steps in TV. Figure 9 shows the reconstructions and Y-slice diagrams of Phantom 3 with 20% noise, where we take 2 terms in NS, 4 iterative steps in LI, 2 iterative steps in CG and 5 iterative steps in TV.

The L^2 errors of these methods in sound speed c_2 are presented at Table 2.

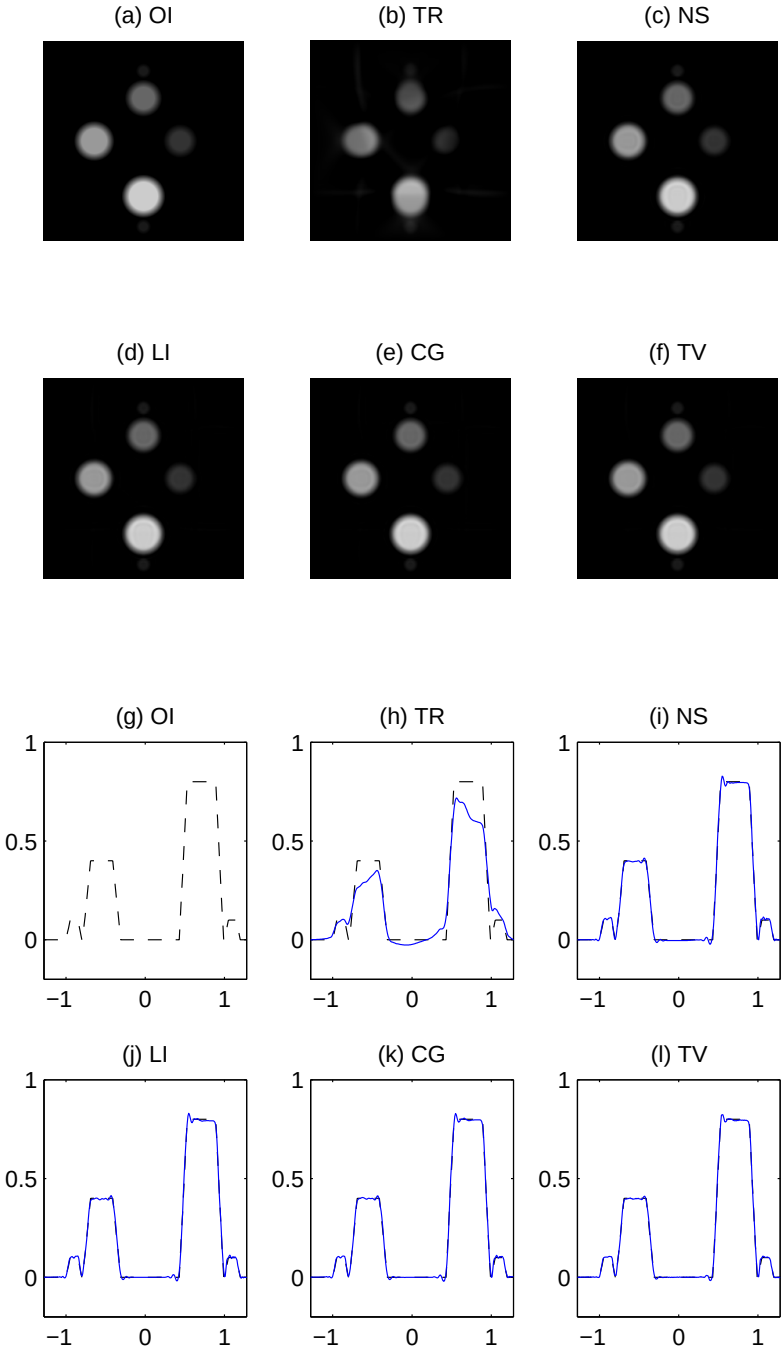

Figure 2: Reconstructions of Phantom 1 in sound speed c_1 with noiseless data. (a-f)The original image and the solutions of TR, NS, LI, CG and TV. (g-l)Y-slices of TR, NS, LI, CG, TV solutions (continuous lines) and the exact solutions (dashed lines).

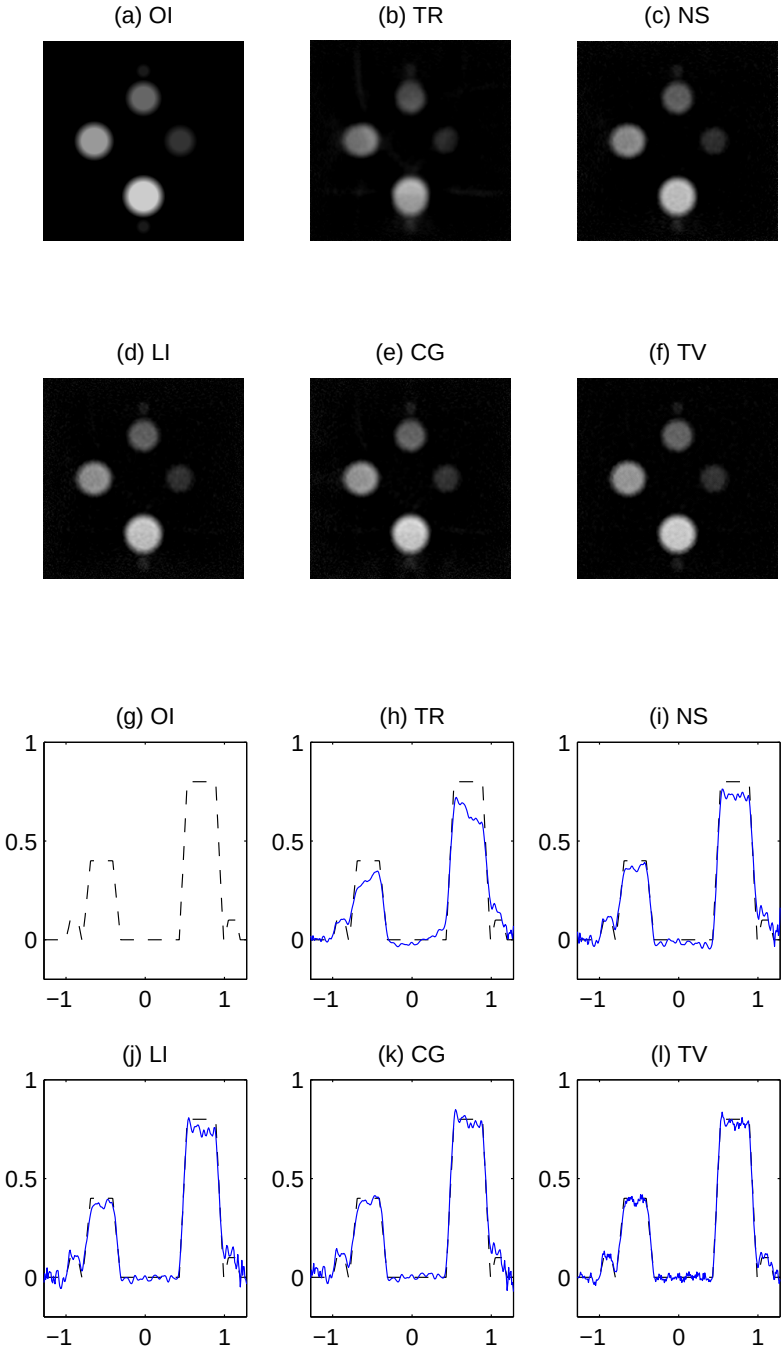

Figure 3: Reconstructions of Phantom 1 in sound speed c_1 with 20% noise. (a-f)The original image and the solutions of TR, NS, LI, CG and TV. (g-l)Y-slices of TR, NS, LI, CG, TV solutions (continuous lines) and the exact solutions (dashed lines).

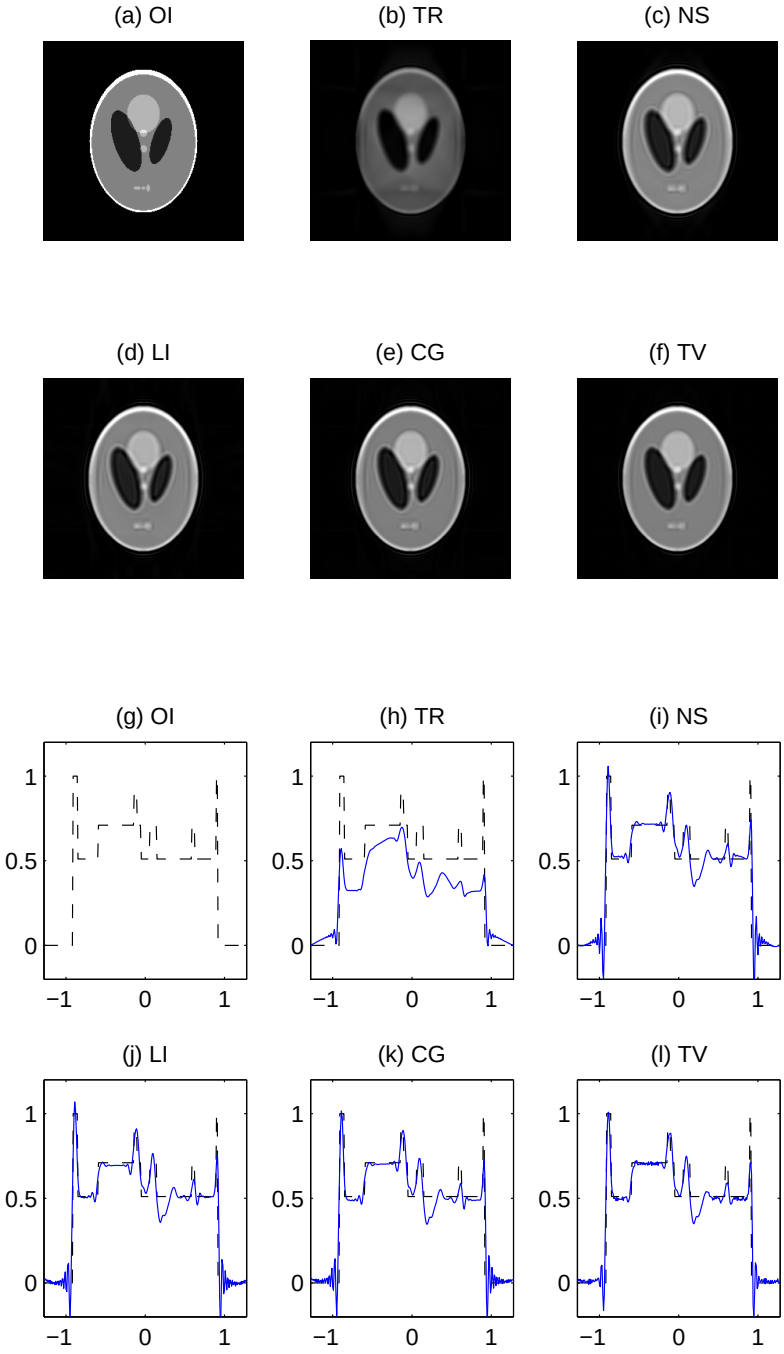

Figure 4: Reconstruction of Phantom 3 in sound speed c_1 with noiseless data. (a-f)The original image and the solutions of TR, NS, LI, CG and TV. (g-l)Y-slices of TR, NS, LI, CG, TV solutions (continuous lines) and the exact solutions (dashed lines).

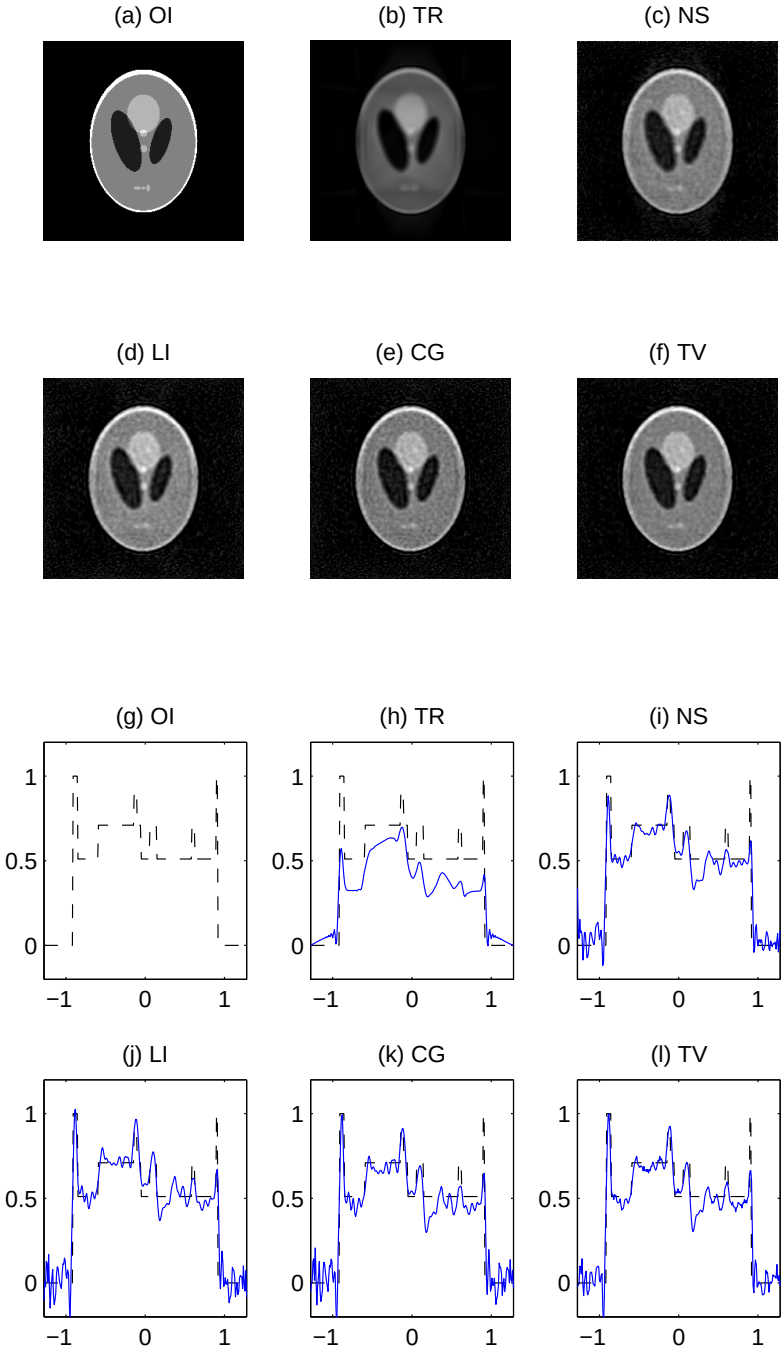

Figure 5: Reconstruction of Phantom 3 in sound speed c_1 with 20% noise. (a-f)The original image and the solutions of TR, NS, LI, CG and TV. (g-l)Y-slices of TR, NS, LI, CG, TV solutions (continuous lines) and the exact solutions (dashed lines).

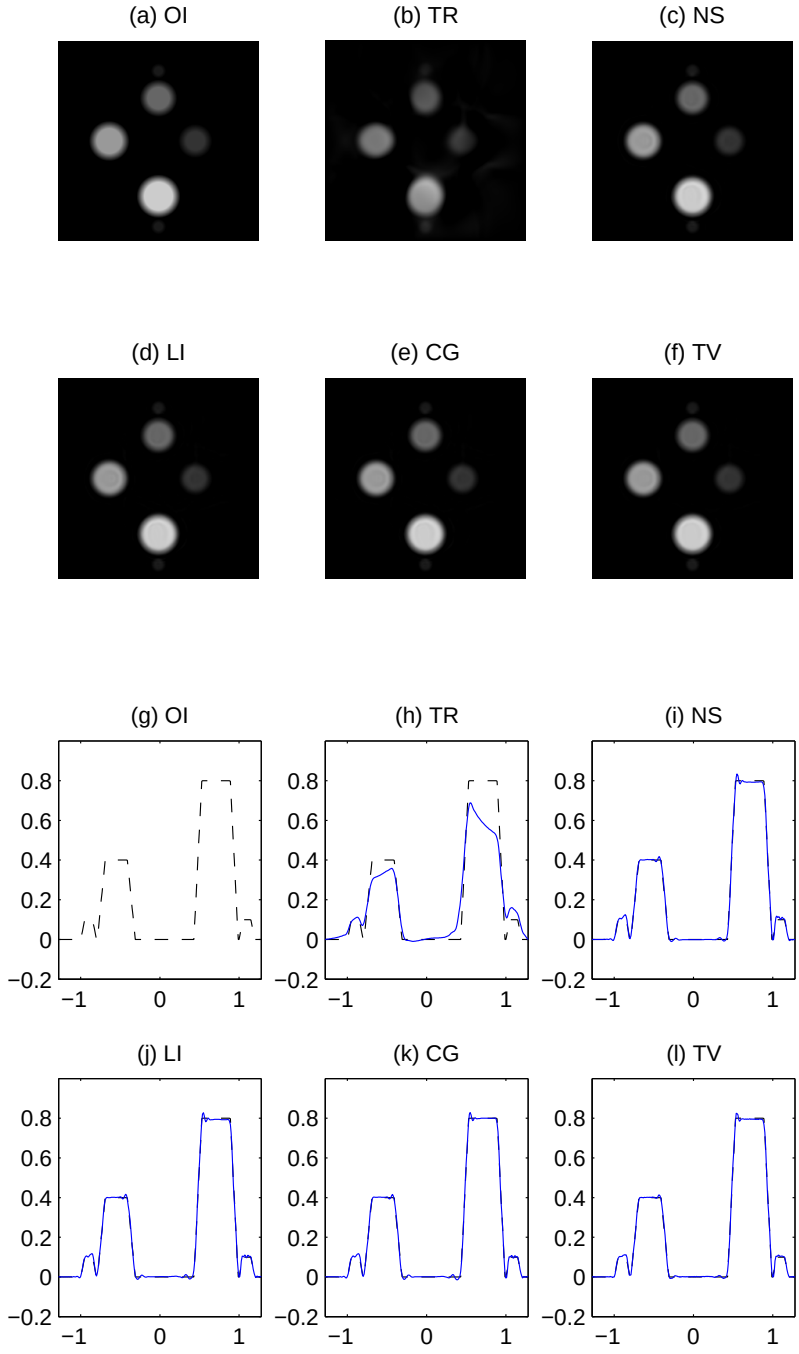

Figure 6: Reconstructions of Phantom 1 in sound speed c_2 with noiseless data. (a-f)The original image and the solutions of TR, NS, LI, CG and TV. (g-l)Y-slices of TR, NS, LI, CG, TV solutions (continuous lines) and the exact solutions (dashed lines).

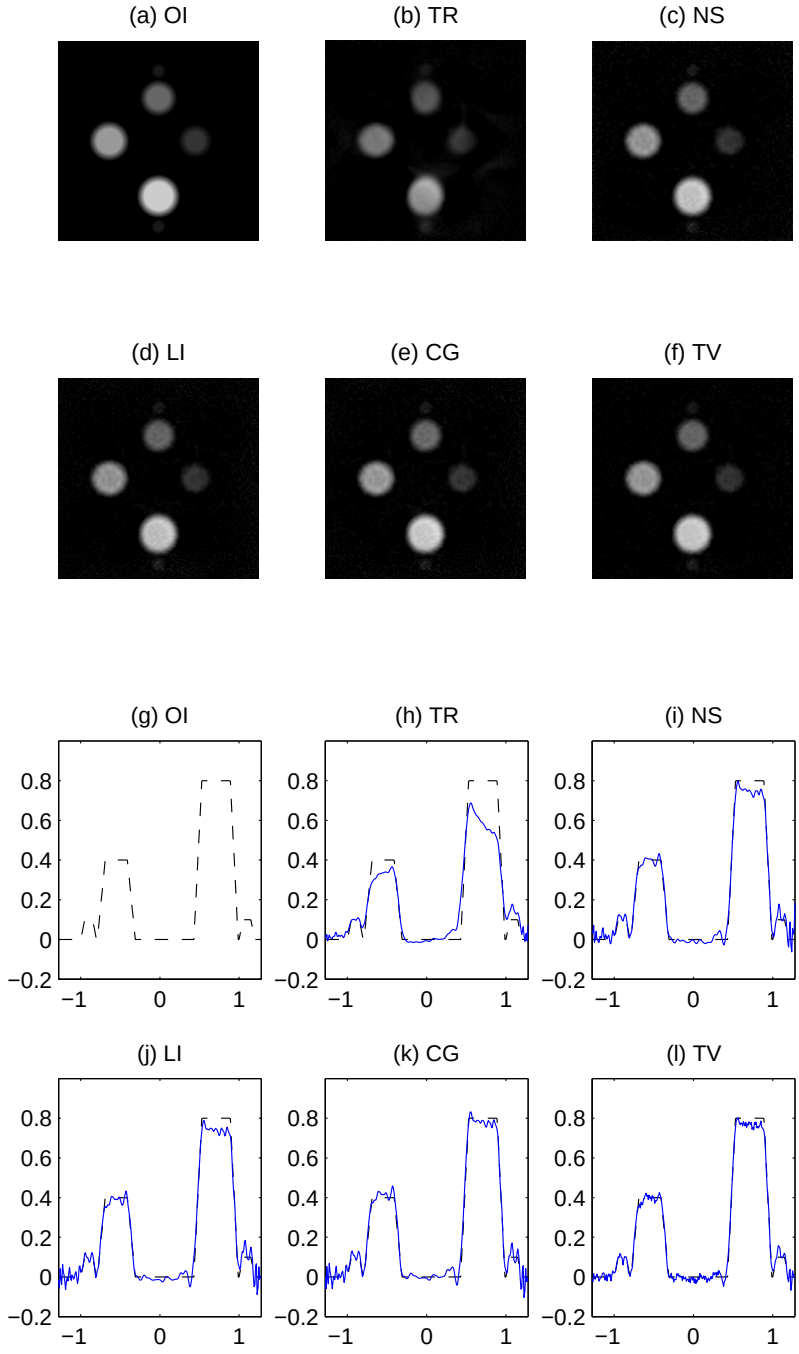

Figure 7: Reconstructions of Phantom 1 in sound speed c_2 with 20% noise. (a-f)The original image and the solutions of TR, NS, LI, CG and TV. (g-l)Y-slices of TR, NS, LI, CG, TV solutions (continuous lines) and the exact solutions (dashed lines).

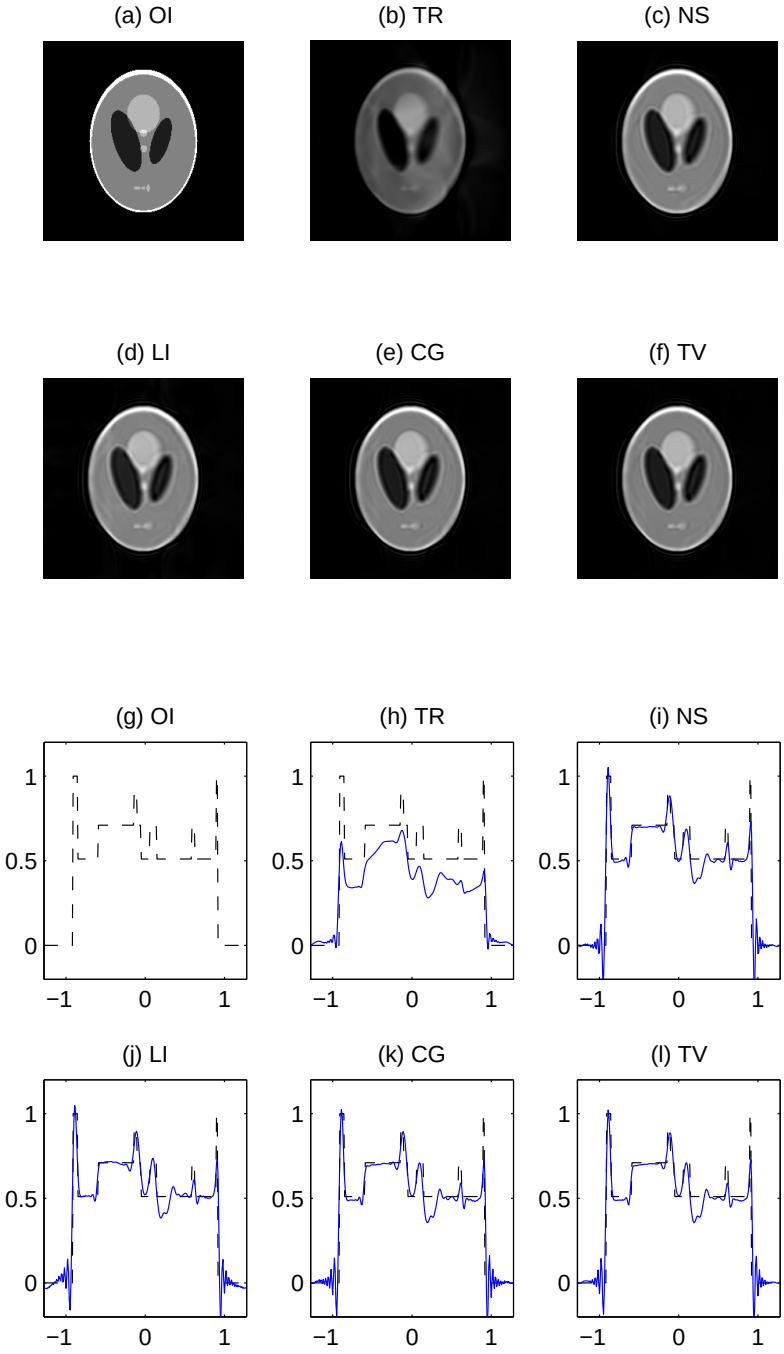

Figure 8: Reconstruction of Phantom 3 in sound speed c_2 with noiseless data. (a-f)The original image and the solutions of TR, NS, LI, CG and TV. (g-l)Y-slices of TR, NS, LI, CG, TV solutions (continuous lines) and the exact solutions (dashed lines).

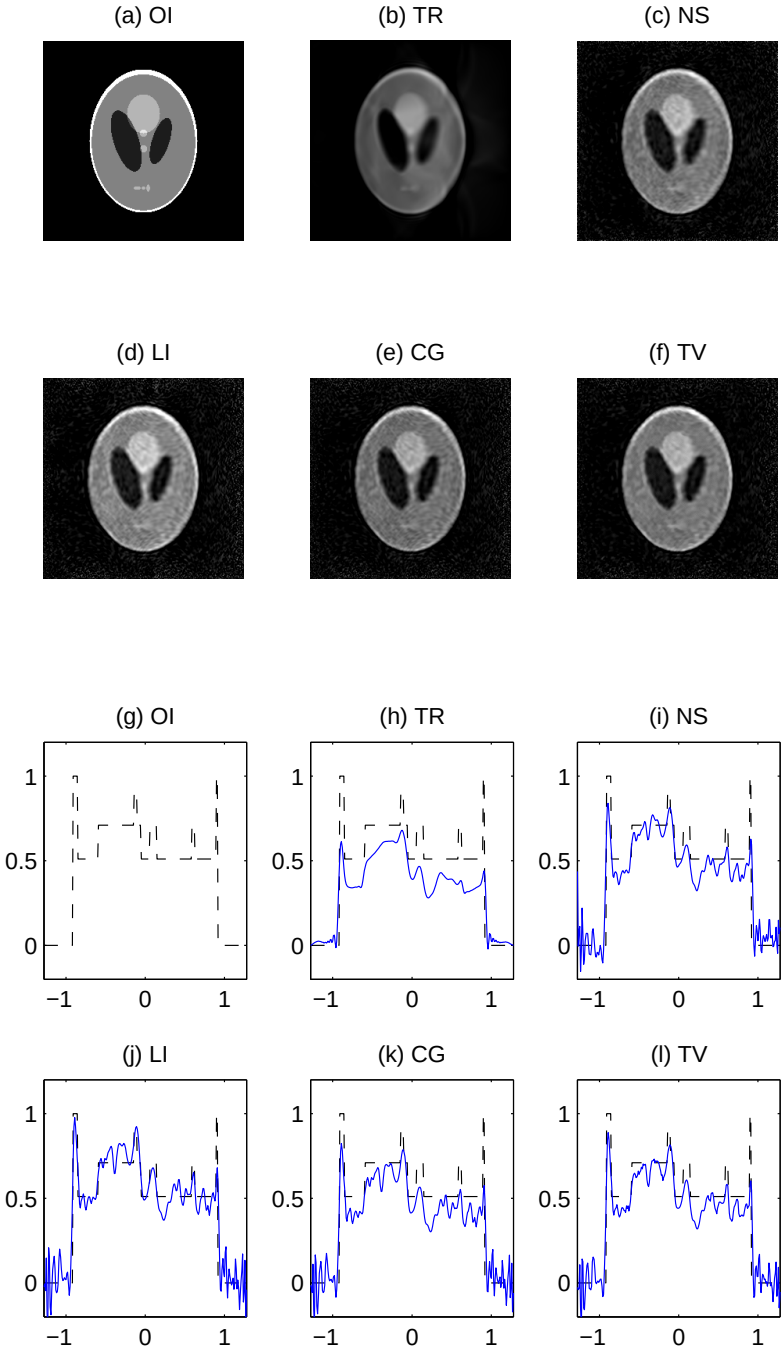

Figure 9: Reconstruction of Phantom 3 in sound speed c_2 with 20% noise. (a-f)The original image and the solutions of TR, NS, LI, CG and TV. (g-l)Y-slices of TR, NS, LI, CG, TV solutions (continuous lines) and the exact solutions (dashed lines).

Phantom	Noise	TR	NS	LI	CG	TV
Phantom 1	noiseless data	32.7%	3.9%	4.1%	4.0%	3.8%
	10% noise	33.0%	11.8%	11.6%	11.3%	7.4%
	20% noise	33.7%	19.5%	19.6%	19.2%	12.8%
Phantom 3	noiseless data	42.9%	26.6%	25.1%	24.9%	25.0%
	10% noise	43.4%	30.3%	29.2%	28.9%	27.4%
	20% noise	42.9%	36.2%	36.9%	36.2%	33.5%

Table 2: L^2 error in sound speed c_2

Phantom	Noise	TR	NS	LI	CG	TV
Phantom 3	noiseless data	42.6%	15.8%	14.9%	14.8%	14.5%
	10% noise	42.9%	22.9%	20.2%	20.4%	16.3%
	20% noise	42.6%	29.0%	28.1%	28.1%	22.0%

Table 3: L^2 error in sound speed c_3

5.3 Sound Speed c_3

In sound speed c_3, we reconstruct Phantom 2. In this sound speed, we can not stably reconstruct the initial value before any bounded time T. However there is a unique solution when $T > 4$ [20]. Therefore, we set $T = 4$ and use $U = [-5.5, 5.5]^2$ as the computation domain.

The reconstructions and Y-slice diagrams with noiseless data are presented in Figure 10, where we take 7 terms in NS, 11 iterative steps in LI, 4 iterative steps in CG and 12 iterative steps in TV. Figure 11 shows the reconstructions and Y-slice diagrams with 20% noise, where we take 2 terms in NS, 4 iterative steps in LI, 2 iterative steps in CG and 8 iteratieve steps in TV.

The L^2 errors of these methods are presented at Table 3.

6 Conclusions

By investigating the adjoint equation with variable sound speed, we propose three image reconstruction algorithms for photoacoustic tomography. These algorithms are executed by iteratively computing the original equation and the adjoint equation. We worked with two dimensional numerical examples and three different sound speeds, including constant sound speed, non-trapping sound speed and trapping sound speed. All the numerical examples demonstrate the well performance of the variational iterative algorithms. Especially, the reconstructions of TV are significantly better than existing inversion methods in the case of the noisy situation.

7 Acknowledgement

The authors are grateful for the helpful discusstions with Professor Shulin Zhou (School of Mathematical Sciences, Peking University) and Qing Han (Department of Mathematics, University of Notre Dame).

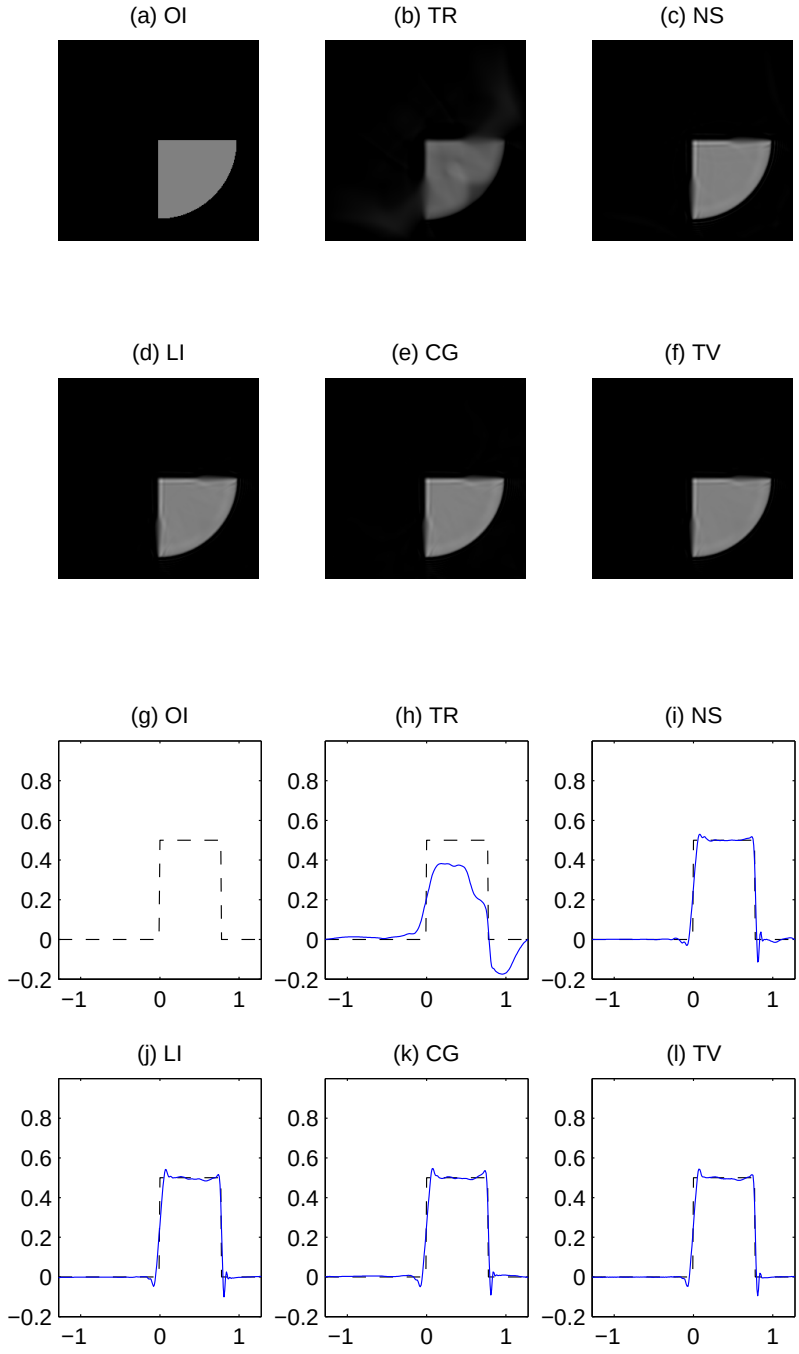

Figure 10: Reconstructions of Phantom 2 in sound speed c_3 with noiseless data. (a-f)The original image and the solutions of TR, NS, LI, CG and TV. (g-l)Y-slices of TR, NS, LI, CG, TV solutions (continuous lines) and the exact solutions (dashed lines).

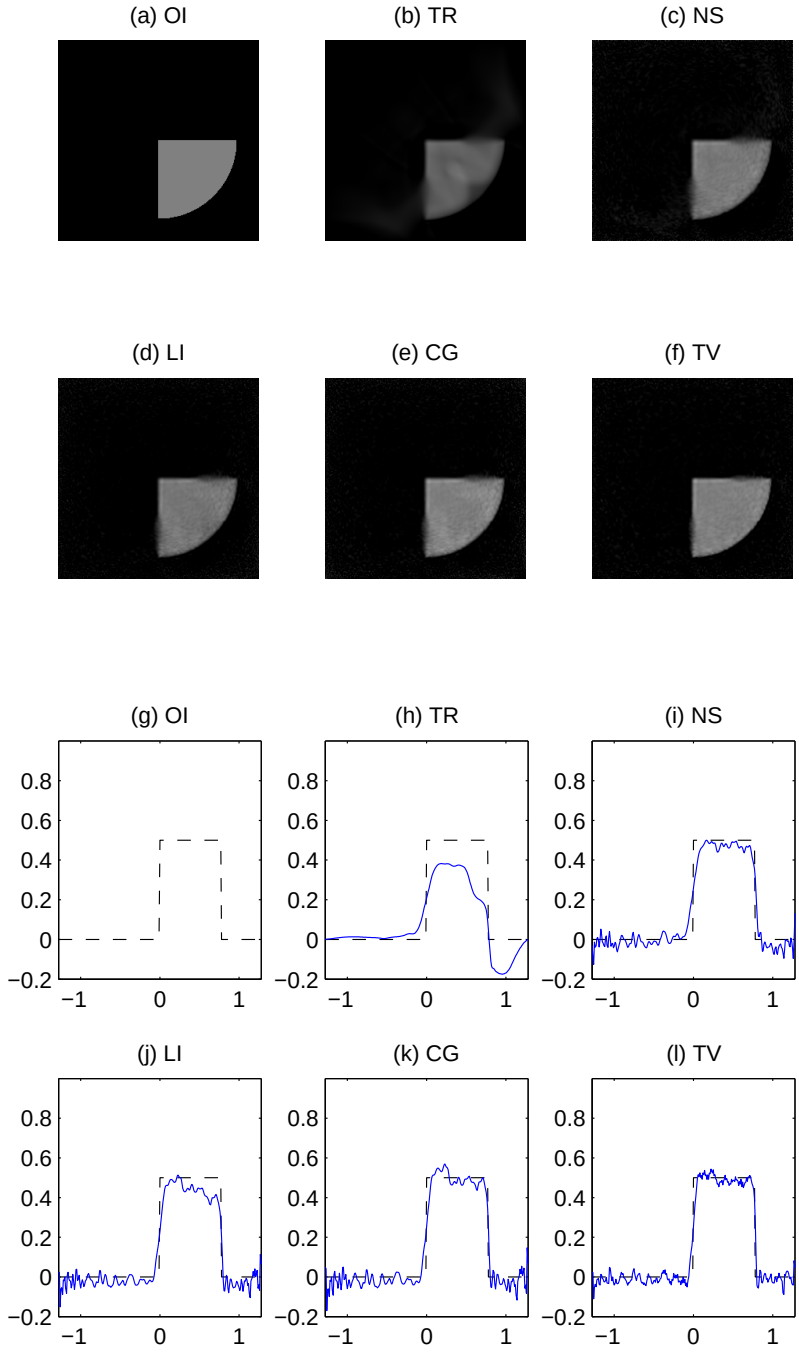

Figure 11: Reconstructions of Phantom 2 in sound speed c_3 with 20% noise. (a-f)The original image and the solutions of TR, NS, LI, CG and TV. (g-l)Y-slices of TR, NS, LI, CG, TV solutions (continuous lines) and the exact solutions (dashed lines).

References

[1] Robert Acar and Curtis R Vogel. Analysis of bounded variation penalty methods for ill-posed problems. *Inverse problems*, 10(6):1217, 1994.

[2] Mark Agranovsky and Peter Kuchment. Uniqueness of reconstruction and an inversion procedure for thermoacoustic and photoacoustic tomography with variable sound speed. *Inverse Problems*, 23(5):2089, 2007.

[3] Xavier Bonnefond and Sébastien Marinesque. Application of a nudging technique to thermoacoustic tomography. *Preprint, arXiv:1112.0654*, 2011.

[4] Peter Burgholzer, Gebhard J Matt, Markus Haltmeier, and Günther Paltauf. Exact and approximative imaging methods for photoacoustic tomography using an arbitrary detection surface. *Physical Review E*, 75(4):046706, 2007.

[5] Evans Lawrence C. *Partial Differential Equations*. American Mathematical Society, 1998.

[6] David Finch and Sarah K Patch. Determining a function from its mean values over a family of spheres. *SIAM journal on mathematical analysis*, 35(5):1213–1240, 2004.

[7] VM Fridman. Method of successive approximations for a fredholm integral equation of the 1st kind. *Uspekhi Matematicheskikh Nauk*, 11(1):233–234, 1956.

[8] Yulia Hristova. Time reversal in thermoacoustic tomography - an error estimate. *Inverse Problems*, 25(5):055008, 2009.

[9] Yulia Hristova, Peter Kuchment, and Linh Nguyen. Reconstruction and time reversal in thermoacoustic tomography in acoustically homogeneous and inhomogeneous media. *Inverse Problems*, 24(5):055006, 2008.

[10] Chao Huang, Kun Wang, Liming Nie, L Wang, and M Anastasio. Full-wave iterative image reconstruction in photoacoustic tomography with acoustically inhomogeneous media. *Transactions on Medical Imaging*, 2013.

[11] Andreas Kirsch. *An Introduction to the Mathematical Theory of Inverse Problems*, volume 120. Springer Verlag, 1996.

[12] Peter Kuchment and Leonid Kunyansky. Mathematics of thermoacoustic tomography. *European Journal of Applied Mathematics*, 19(02):191–224, 2008.

[13] Leonid Kunyansky. A series solution and a fast algorithm for the inversion of the spherical mean radon transform. *Inverse Problems*, 23(6):S11, 2007.

[14] Leonid Kunyansky. Fast reconstruction algorithms for the thermoacoustic tomography in certain domains with cylindrical or spherical symmetries. *Inverse Problems and Imaging*, 2011.

[15] Louis Landweber. An iteration formula for fredholm integral equations of the first kind. *American journal of mathematics*, 73(3):615–624, 1951.

[16] Dimple Modgil, Mark A Anastasio, and Patrick J La Rivière. Image reconstruction in photoacoustic tomography with variable speed of sound using a higher-order geometrical acoustics approximation. *Journal of biomedical optics*, 15(2):021308–021308, 2010.

[17] Jianliang Qian, Plamen Stefanov, Gunther Uhlmann, and Hongkai Zhao. An efficient neumann series-based algorithm for thermoacoustic and photoacoustic tomography with variable sound speed. *SIAM Journal on Imaging Sciences*, 4(3):850–883, 2011.

[18] Karim Ramdani, Takéo Takahashi, and Marius Tucsnak. Uniformly exponentially stable approximations for a class of second order evolution equations. *ESAIM: Control, Optimisation and Calculus of Variations*, 13(03):503–527, 2007.

[19] Leonid I Rudin, Stanley Osher, and Emad Fatemi. Nonlinear total variation based noise removal algorithms. *Physica D: Nonlinear Phenomena*, 60(1):259–268, 1992.

[20] Plamen Stefanov and Gunther Uhlmann. Thermoacoustic tomography with variable sound speed. *Inverse Problems*, 25(7):075011, 2009.

[21] Plamen Stefanov and Gunther Uhlmann. Thermoacoustic tomography arising in brain imaging. *Inverse Problems*, 27(4):045004, 2011.

[22] Curtis R Vogel. *Computational methods for inverse problems*, volume 23. Society for Industrial Mathematics, 1987.

[23] Minghua Xu and Lihong V Wang. Universal back-projection algorithm for photoacoustic computed tomography. *Physical Review E*, 71(1):016706, 2005.

[24] Minghua Xu and Lihong V Wang. Photoacoustic imaging in biomedicine. *Review of scientific instruments*, 77(4):041101–041101, 2006.

[25] Yuan Xu and Lihong V Wang. Effects of acoustic heterogeneity in breast thermoacoustic tomography. *Ultrasonics, Ferroelectrics and Frequency Control, IEEE Transactions on*, 50(9):1134–1146, 2003.

[26] Yuan Xu and Lihong V Wang. Time reversal and its application to tomography with diffracting sources. *Physical review letters*, 92(3):033902, 2004.